

On the mechanics of inhaled bronchial transmission of pathogenic microdroplets generated from the upper respiratory tract, with implications for infection onset

Saikat Basu *

Department of Mechanical Engineering, South Dakota State University, Brookings, South Dakota 57007, USA

(Dated: June 27, 2024)

Could the microdroplets formed by viscoelastic stretching and break-up of mucosal liquids in the upper respiratory tract (URT), when inhaled further downwind through the airway, explain the brisk pace at which deep lung infections emerge following the onset of initial infection at the URT? While it is well-established that particulates inhaled from outside can possibly penetrate to the lower airway only if they are smaller than approximately $5\ \mu\text{m}$, the fate of particulates (many exceeding $5\text{-}\mu\text{m}$ in diameter) that are sheared away from the intra-URT mucosa during inhalation remains an open question. These particulates predominantly originate in the region encompassing the nasopharynx, the oropharynx, and the laryngeal chamber with the vocal folds. To resolve the posed question, this study considers a computed tomography-based three-dimensional anatomical airway reconstruction and isolates the tract from the laryngeal vocal fold region (superior to the glottis), mapping the entire tracheal cavity and concluding at the second generation of the tracheobronchial tree in the lower airway. Through the delineated geometry, airflow simulation is conducted using the Large Eddy Simulation scheme to replicate relaxed inhalation at a rate of 15 L/min. Against the ambient air flux, representative numerical experiments have been performed to monitor the transport of liquid particulates (aerosols/droplets) with diameters ranging from $1\ \mu\text{m}$ to $30\ \mu\text{m}$, bearing physical properties akin to aerosolized mucus containing embedded virions. The full-scale numerically predicted transmission trends to the lower airway were found consistent with the findings from a reduced-order mathematical model that conceptualized the impact of intra-airway vortex instabilities on local particle transport through use of point vortex idealization in an anatomy-guided two-dimensional potential flow domain. The results collectively demonstrate markedly elevated trends of deep lung penetration by the URT-derived particulates, even if they are as large as $10\ \mu\text{m}$ and $15\ \mu\text{m}$. The high viral load physically carried by such droplets to the bronchial spaces could mechanistically explain the accelerated seeding of infection in the lungs.

I. INTRODUCTION

When inhaled air sweeps past the mucociliary coating of the upper respiratory tract (URT), it is plausible to hypothesize that the interfacial interactions would lead to localized viscoelastic stretching and break-up of mucosal layers resulting in the formation and release of microdroplets, which would then be pushed downwind by the air streamlines. For instance, it is key to note the prominent instability effects when the viscoelastic layer (mucus) resting on a viscous fluid film (serous fluid) is exposed to the incoming airflow [1]. The *ansatz* is also supported by the established literature that has examined the reverse process: exhalation [2–5]. The expiratory transport regimes, even during silent breathing, emit liquid particulates that span a wide range of length scales [6]. From such paradigm, if we now pivot our attention to inhaled (i.e., *into* the airway) transport, some immediate questions that come forth concern the fate of the intra-URT particulates generated during inhalation and their probable relevance in progressive disease transmission, especially to the deep lungs. On that note, the present study, through numerical experiments performed in a three-dimensional anatomical airway reconstruction and with simulation-informed reduced-order analytical modeling in an anatomy-inspired two-dimensional channel, attempts to answer the following main queries:

- Q_1 . When inhaled from outside, it is well-known that the dominant inertial motion of the particulates larger than $5\ \mu\text{m}$ ensures that hardly any of them, *albeit* potentially none at all, would penetrate to the lower airway. But is such conclusion also true for particulates of similar sizes generated through mucus separation from the URT surface during inhalation?
- Q_2 . What is the viral load transmitted by particulates sheared away from the URT, that may manage to penetrate to the deep lungs, and more specifically, how does the viral transmission trend correlate with particulate sizes?

* Saikat.Basu@sdsu.edu

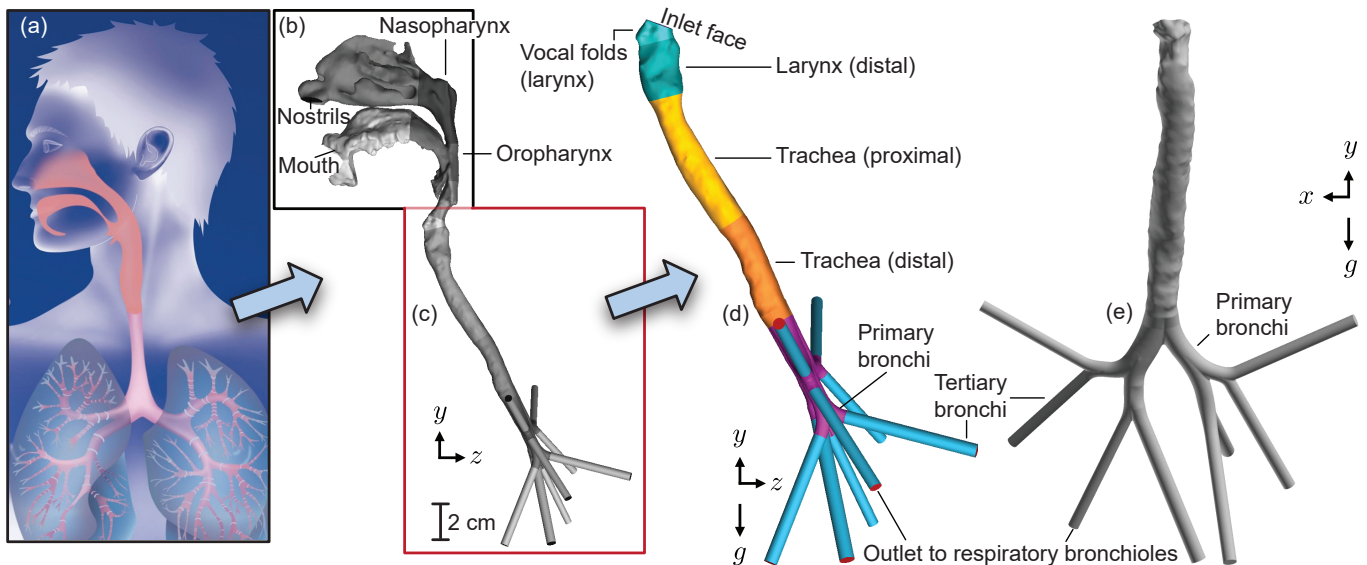


FIG. 1. (a) A demonstrative cartoon of the human respiratory system, encompassing the upper respiratory tract, the mouth, and the lower respiratory tract, extending till the deep lungs. The visual is adopted with copyrights' permission from the Getty Images[®]. (b-c) Sample computed tomography (CT) imaging-based reconstruction of an adult human airway. It serves as a three-dimensional anatomically realistic equivalent of the cartoon in panel (a), with regions included till generation 2 (tertiary bronchi) of the tracheobronchial tree. The domain within the red box, i.e., panel (c), is isolated for the numerical experiments on inhaled downwind transport of microdroplets generated from the upper respiratory tract. The isolated region is additionally shown in panel (d) for the sagittal view with anatomical demarcations and in panel (e) for the coronal view. The symbol g signifies the gravity direction in the numerical simulations and the subsequent analytical framework, with x , y , and z defining the spatial orientation of the test cavity. Box (c) additionally highlights the precise length scale of the geometry.

This study addresses Q_1 through full-scale numerical tracking of inhaled constituents inside an anatomically accurate airway geometry with a supporting reduced-order mathematical model of the system. Next for Q_2 , it connects the fluid dynamics findings with virological parameters, such as the sputum viral concentration [7] for a representative pathogen (SARS-CoV-2), and critiques the projected viral load transmitted to the bronchial pathways in light of the verified infectious dose of the pathogen [8, 9]. The resulting translational analysis helps assess the proclivity for deep lung infection driven by inhalation of aerosolized intra-URT mucosal remnants. It is worth noting that this *in silico* approach, rooted in the underlying respiratory flow physics as discussed here, is agnostic to any virus specificity and is potentially extensible to other respiratory pathogens by integrating the fluid mechanics outcomes of inhaled transport with appropriate virological, epidemiological, and immunological data. In that context, this work could advance an emerging niche sub-field that brings together classical fluid dynamics and virology [10–12]. For select recent relevant studies on deep lung kinetics and pathophysiology, the reader may refer to [13–17].

II. METHODS

A. Numerical modeling of inhaled transport of microdroplets generated in the upper respiratory tract

As is the case for inhaled transport of microdroplets (also referred to as particulates, or equivalently, simply as particles in this exposition) through the respiratory cavity, in numerical simulations involving the dispersion of small particles under dilute conditions—the common approach assumes one-way coupling. This reduction implies that while the airflow continuum carries the particulates, the impact of such particulates on the underlying flow regimes could be disregarded. Consequently, the ambient airflow field is initially resolved, and the flow outcomes are subsequently employed to numerically solve the relevant particle equations of motion.

In this study, we have used Large Eddy Simulation (LES) scheme with dynamic subgrid-scale kinetic energy transport model to numerically replicate the inhaled air flux through an anatomically realistic airway reconstruction. To model the inhaled particle transport therein, we have applied the Lagrangian approach which is more suitable (compared to the Eulerian methods) for the dilute suspension of relatively large particles for which inertia could

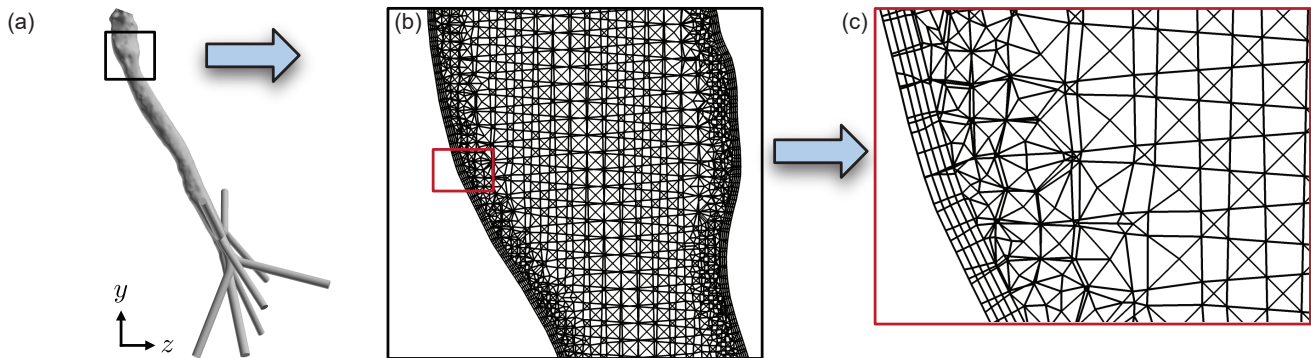


FIG. 2. The black box in panel (a) marks the location of the demonstrated mesh region mapping a sagittal cross-section running mid-way through the test cavity (shown henceforth in Fig. 3). Panels (b) and (c) present multi-scale visuals of the mesh. In specific, panel (c) highlights the four layers of pentahedral cells used for near-wall refinement to ensure reliable numerical tracking of particle deposition.

often be dominant in determining the spatial trajectories and eventual deposition spots. The simulated airflow field is coupled with the Lagrangian particle transport analysis to derive the intra-airway deposition and penetration trends.

1. Anatomical geometry reconstruction and spatial discretization

From de-identified, high-resolution, medical-grade computed tomography (CT) imaging, this study has first reconstructed a complete three-dimensional adult respiratory airway [18]; see Fig. 1a-c. The extraction warranted a radio-density thresholding between -1024 to -300 Hounsfield units [19, 20] to capture the airspace from the CT slices. Aiming to address Q_1 and Q_2 (posed in §I), the reconstruction has then been digitally redacted to focus on the space mapping the vocal fold region of the larynx (space with highest concentration of liquid particulates formed from intra-URT mucosal break-up) along with the distal laryngeal chamber, the trachea, and the lower airway extending till generation 2 of the tracheobronchial tree, with primary and tertiary bronchi, followed by the respiratory bronchiolar outlets as entry to the deeper recesses of the lungs. See Fig. 1d-e for the anatomical test geometry with the described regions marked out. To prepare the domain for numerical simulations, the test cavity was spatially segregated into 2.5 million graded, unstructured, tetrahedral elements, along with four layers of pentahedral cells (with 0.025-mm height for each cell and an aspect ratio of 1.1) extruded at the airway cavity walls [21] to resolve the near-wall particulate dynamics; see Fig. 2.

While using the LES scheme, a finer mesh refinement typically leads to more precise outcomes. For instance, at the upper limit, achieving results akin to Direct Numerical Simulation (DNS) is possible if the grid dimensions are smaller than the Kolmogorov scale, \mathcal{K} , which is defined as follows [22]:

$$\mathcal{K} = \left(\frac{\nu^3}{\varepsilon} \right)^{1/4}, \quad (1)$$

with ε as the turbulence dissipation rate and ν being the fluid kinematic viscosity. Another length scale of note is the Taylor scale, λ , which typically exceeds \mathcal{K} and is defined as

$$\lambda = \left(\frac{10\nu k}{\varepsilon} \right)^{1/2}, \quad (2)$$

with k being the turbulence kinetic energy. From the simulation data of the inhaled airflow field from this study, it is seen that both λ and \mathcal{K} collapse to $\mathcal{O}(10^{-4})$ m, while the mean grid scale is also $\rightarrow \mathcal{O}(10^{-4})$ m, suggesting that the test grid has been sufficiently resolved for precise estimation of the transport parameters.

2. Numerical simulation of inhaled airflow

We have employed the LES approach to numerically model the inhaled airflow, with eddies exceeding the grid scale explicitly resolved, whereas those that are smaller than the grid scale are approximated. Specifically, fluctuations

below the grid size, referred to as subgrid scales, are filtered out, and their impact on larger scales is replicated through modeling. Assuming incompressible and isothermal conditions for the inhaled air flux, the filtered continuity and Navier–Stokes equations are respectively as follows:

$$\frac{\partial}{\partial x_i} (\rho \bar{u}_i) = 0 \quad (3)$$

and

$$\frac{\partial \bar{u}_i}{\partial t} + \frac{\partial}{\partial x_j} (\bar{u}_i \bar{u}_j) = -\frac{1}{\rho} \frac{\partial \bar{p}}{\partial x_i} + \frac{\partial}{\partial x_j} \left(\nu \frac{\partial \bar{u}_i}{\partial x_j} \right) - \frac{\partial \tau_{ij}}{\partial x_j}. \quad (4)$$

Here \bar{u}_i represents the filtered (i.e., resolved) velocity, \bar{p} is the filtered pressure, ν and ρ are respectively the kinematic viscosity and the density of inhaled warmed-up air, and τ_{ij} is the subgrid scale (SGS) stress tensor defined by

$$\tau_{ij} - \frac{1}{3} \tau_{kk} \delta_{ij} = -\nu_{sgs} \left(\frac{\partial \bar{u}_i}{\partial x_j} + \frac{\partial \bar{u}_j}{\partial x_i} \right), \quad (5)$$

where ν_{sgs} is the SGS kinematic viscosity and δ_{ij} is the Kronecker delta. It is to be noted that τ_{kk} , which comprises the isotropic part of the SGS stresses, is not modeled but added to the filtered static pressure. Subsequently, the instantaneous field velocity is given by

$$u_i = \bar{u}_i + u_i^{sgs}, \quad (6)$$

with u_i^{sgs} representing the SGS velocity fluctuations. The flow patterns and particle dispersion within the human respiratory system will be strongly impacted by the secondary flows common in such complex geometries and by the airflow transitions between laminar and turbulent regimes. To simultaneously capture the transitional features as well as the secondary flow formations, this study uses the dynamic subgrid-scale kinetic energy transport model [23–25]. Therein the SGS kinematic viscosity, ν_{sgs} , is obtained from the Kolmogorov-Prandtl hypothesis [26] in the following form:

$$\nu_{sgs} = C_k k_{sgs}^{1/2} \Delta_f. \quad (7)$$

In the above equation, C_k is a constant value and Δ_f is the filter size computed as $\Delta_f \equiv (\text{grid cell volume})^{1/3}$. The term k_{sgs} represents the SGS kinetic energy, defined by

$$k_{sgs} = \frac{1}{2} (\overline{u_i u_j} - \bar{u}_i \bar{u}_j). \quad (8)$$

To derive k_{sgs} , we solve the following filtered transport equation:

$$\frac{\partial k_{sgs}}{\partial t} + \frac{\partial}{\partial x_j} (k_{sgs} \bar{u}_j) = \frac{\partial}{\partial x_j} \left(\nu_{sgs} \frac{\partial k_{sgs}}{\partial x_j} \right) + \frac{\partial \bar{u}_i}{\partial x_j} \left[\nu_{sgs} \left(\frac{\partial \bar{u}_i}{\partial x_j} + \frac{\partial \bar{u}_j}{\partial x_i} \right) - \frac{2}{3} k_{sgs} \delta_{ij} \right] - C_\varepsilon \frac{k_{sgs}^{3/2}}{\Delta_f}, \quad (9)$$

with the model constants in the previous equations, i.e., C_k and C_ε , being determined dynamically [23].

Applying the LES scheme as described above, the inhaled airflow through the anatomical airspace was replicated for 15 L/min inhalation rate [27]. See Fig. 1d for the pressure inlet face at the location of vocal folds in the larynx and for the pressure outlets at the distal ends of the reconstructed generation 2 bronchial tubes. Enforcing no slip (i.e., zero velocity) boundary condition at the airway walls, the pressure gradient-driven simulation used time-steps of 0.0002 s [25], which is smaller than the Kolmogorov time scale $= (\nu/\varepsilon)^{1/2}$ [22], for a flow solution time of 0.35 s. The simulation was executed on a segregated solver with pressure-velocity coupling and second-order upwind spatial discretization. The eventual solution convergence was monitored by minimizing the mass continuity residual to $\mathcal{O}(10^{-3})$ and the velocity component residuals to $\mathcal{O}(10^{-6})$. Also, considering the warmed-up state of inhaled air passing through the respiratory pathway, the air density ρ was set at 1.204 kg/m³ in the simulations, with 18.218×10^{-6} m²/s as its kinematic viscosity ν .

3. Numerical experiments for particulate transport

Against the solved airflow field, the particulates assumed to be formed from intra-URT mucus break-up were tracked from the vocal fold region of the larynx (see the marked inlet face in Fig. 1d). The air-particle phases were one-way

coupled with the particles being impacted by the ambient flow field; the underlying flow domain was considered quasi-steady while evaluating the particle transport parameters. Lagrangian-based inert discrete phase model, with a Runge-Kutta solver, was used to numerically integrate the particle transport equation:

$$\frac{du_{pi}}{dt} = \frac{18\mu}{d^2\rho_p} \frac{C_D Re_p}{24} (u_i - u_{pi}) + g_i \left(1 - \frac{\rho}{\rho_p}\right) + F_i. \quad (10)$$

Here u_{pi} represents the particulate velocity, ρ_p is the material density of the particulates, d represents the particulate diameter, Re_p is the particulate Reynolds number, g_i signifies the gravitational acceleration in the i direction, C_D is the drag coefficient, and F_i is any other additional body forces per unit particulate mass, e.g., the Saffman lift force exerted by a typical flow-shear field on small particulates transverse to the airflow direction. In this context, note that the solution scheme considered the particulates to be large enough to ignore any Brownian motion effects on their dynamics.

To evaluate the drag term (i.e., the co-factor on the first term) on the right hand side of equation 10, the quantities Re_p and C_D are respectively computed as

$$Re_p = \frac{\rho_p d |u_i - u_{pi}|}{\mu}, \quad C_D = a_1 + \frac{a_2}{Re_p} + \frac{a_3}{Re_p^2}, \quad (11)$$

where μ is the molecular viscosity of the ambient fluid (i.e., air), while a_1 , a_2 , and a_3 are functions of Re_p determined based on the spherical drag law [28]. Subsequently, the particulate trajectories are derived from their spatiotemporal locations, $x_i(t)$, obtained by numerical integration of the following velocity vector equation:

$$u_{pi} = \frac{dx_i}{dt}. \quad (12)$$

Intra-airway aerial tracking of a particulate pathline was stopped once it entered the mesh element layer adjacent to the enclosing walls of the respiratory cavity. The particulates escaping through the bronchiolar outlets were also recorded, and represented the particulates penetrating to the respiratory bronchioles and deep lungs. The numerical experiments in this study tested particulates of diameters 1 – 30 μm (with increments of 1 μm). In total, $\mathcal{N} = 1622$ particulates of each size were tracked; \mathcal{N} being the number of surface elements in the mesh layer mapping the inlet face (see Fig. 1). Also, considering that saliva-mixed mucus is 99.5% water [29], the material density of the particulates was assumed to be $\rho_p = 1.00175$ g/ml, approximated as the weighted average (see equation 13 below) between 99.5% water and the residual pathogenic and biological non-volatile compounds with a representative density of $\rho_{nv} = 1.35$ g/ml; e.g., for protein [30], the density being independent of the nature of the protein and particularly independent of its molecular weight. The weighted average calculation for the simulated particulate density is as follows:

$$\rho_p = \frac{0.5 \times \rho_{nv} + 99.5 \times \rho_w}{100}, \quad (13)$$

with $\rho_w = 1.0$ g/ml representing the density of water. The consideration of inertness for the tracked particulates (per equation 10) also implies that the modeling framework was agnostic to the biological nuances of the embedded constituents in the particulates, beyond the imposition of the appropriate physical properties, e.g., density. The modeling approach also discounted any heat transfer effects between the flow constituents and the surrounding tissues enclosing the anatomical airspace.

B. Analytical model for inhaled airflow and particulate transport

To verify the particulate transport trends to the bronchial domain as derived numerically, this study invokes a simulation-informed reduced-order analytical model (S-ROAM), with a two-dimensional channel mimicking the laryngotracheal domain. Therein, the inhaled airflow was modeled in the dimensionless complex χ plane, with $\chi = \alpha + i\beta$ and $i\beta$ aligned with the channel's streamwise axis; see Fig. 3. The two-dimensional channel had its streamwise length and cross-stream width based on the averaged dimensions of the anatomical tract from Fig. 3a-b. The channel walls were placed at $\alpha = 0, 1$. Based on the geometric inputs, the S-ROAM enforced $L/W \approx 9$, where L represents the streamwise channel length and W is the inlet width. For additional details on the analytical approach, see our recent paper [31].

The reduced system modeled an extended vortex patch emerging in the full-scale numerical simulation as a collection of five point vortices distributed over the area of the simulated vortex core (on the channel plane, mapping the mid-sagittal section of the three-dimensional cavity; see Fig. 3b), bearing dimensionless circulations $\Gamma_i = \omega A/5UW$,

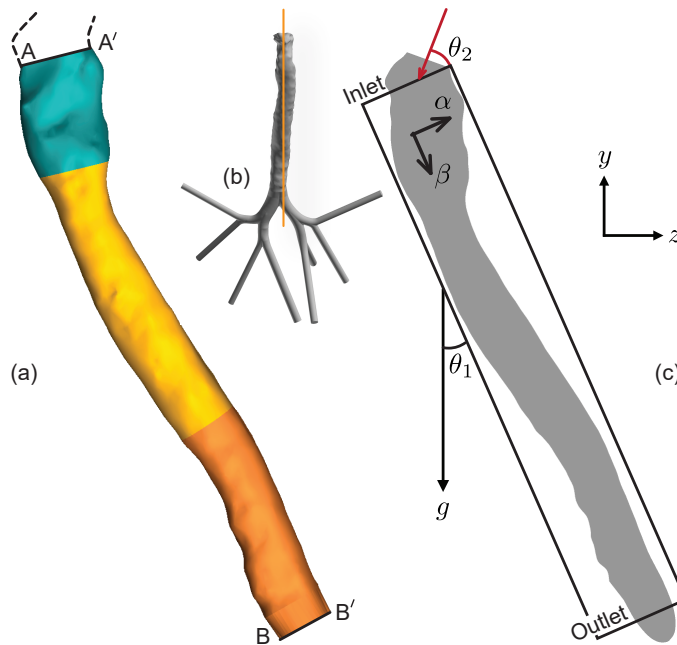


FIG. 3. (a) Laryngotracheal region upwind from the primary bronchi used to develop a simulation-informed reduced-order analytical model (S-ROAM) for bronchial transmission. AA' marks the distal larynx upwind face and BB' marks the downwind face of the distal tracheal cavity; see labels in Fig. 1d. The cross-sectional areas of the cavity at AA' and BB' are 108.61 mm^2 and 123.03 mm^2 , respectively. The corresponding hydraulic diameters are 11.03 mm and 12.20 mm , respectively. The linear spatial distance between the two faces is approximately 115.84 mm , at angle $\theta_1 = 23.77^\circ$ to the vertical (direction of gravity in the numerical simulations). Panel (b) highlights the location and orientation of the planar cross-section shown in panel (c) and also previously as the location of the mesh visuals in Fig. 2. The vortex strengths and positions for the S-ROAM are extracted from the simulated data mapping this two-dimensional plane; the plane cuts through the entire cavity of panel (a). $\theta_2 = 33.94^\circ$ is the assumed angle in S-ROAM, at which microdroplets enter the AA' inlet face and is governed by the anatomical shape of the cavity upwind from AA' (marked by the dashed black traces; also see Fig. 1).

where ω was the mean vorticity (as determined from the numerical simulations) spread over the patch area A and U is the characteristic streamwise air speed through the channel. From the simulated data, we had: $\omega = 1750 \text{ s}^{-1}$, $A = 2.65 \times 10^{-5} \text{ m}^2$, and $U = Q/a = 2.16 \text{ m/s}$, with $a = 115.82 \text{ mm}^2$ being the area of the inlet face and $Q = 15 \text{ L/min} = 0.00025 \text{ m}^3/\text{s}$ being the simulated inhalation flux. The anatomical planar section from which the vorticity information was extracted is shown in Fig. 3c.

In the S-ROAM, the straight streamlines at the channel walls were established through inclusion of periodic images of the point vortices in the cross-stream α direction. The resulting (dimensionless) complex potential for this system, with a dimensionless background speed of unity, is [32–34]:

$$F(\chi) = \phi(\alpha, \beta) + i\psi(\alpha, \beta) = i\chi + \sum_{i=1}^5 \frac{\Gamma_i}{2\pi i} \log \left\{ \frac{\sin[\pi(\chi - \chi_i)/2]}{\sin[\pi(\chi + \chi_i^*)/2]} \right\}, \quad (14)$$

with ϕ as the velocity potential and ψ as the real-valued flow streamfunction; the asterisk denotes complex conjugation. Subsequently, the inhaled particulate motion was analytically derived using a simplified version of the Maxey-Riley equation [35], in the two-dimensional vector form [36, 37]:

$$\frac{d\mathbf{w}}{dt} = - \left[\mathbf{J} + \frac{2St^{-1}}{3(\sigma+1)} \mathbf{I} \right] \cdot \mathbf{w} + \frac{\sigma}{\sigma+1} \left(Fr^{-2} \mathbf{g} - \frac{D\mathbf{u}}{Dt} \right). \quad (15)$$

Here \mathbf{u} is the local fluid velocity in vector coordinates, $\mathbf{w} = \mathbf{u}_p - \mathbf{u}$ is the relative velocity of a particulate with velocity \mathbf{u}_p , \mathbf{J} is the two-dimensional Jacobian matrix, \mathbf{I} is the identity matrix, \mathbf{g} implies gravity, with the nondimensional parameters being Stokes number $St \equiv d^2U/18\nu L$, Froude number $Fr \equiv U/\sqrt{gL}$, and $\sigma \equiv 2(\rho_p - \rho)/3\rho$.

Although viscous effects are neglected in the above velocity model, particle drag is included. This form of the model ignores the Faxen correction terms and the Basset-Boussinesq history force. Particulates are assumed to be entering the S-ROAM domain (inclined at an angle $\theta_1 = 23.77^\circ$ to the direction of gravity, per the general shape and

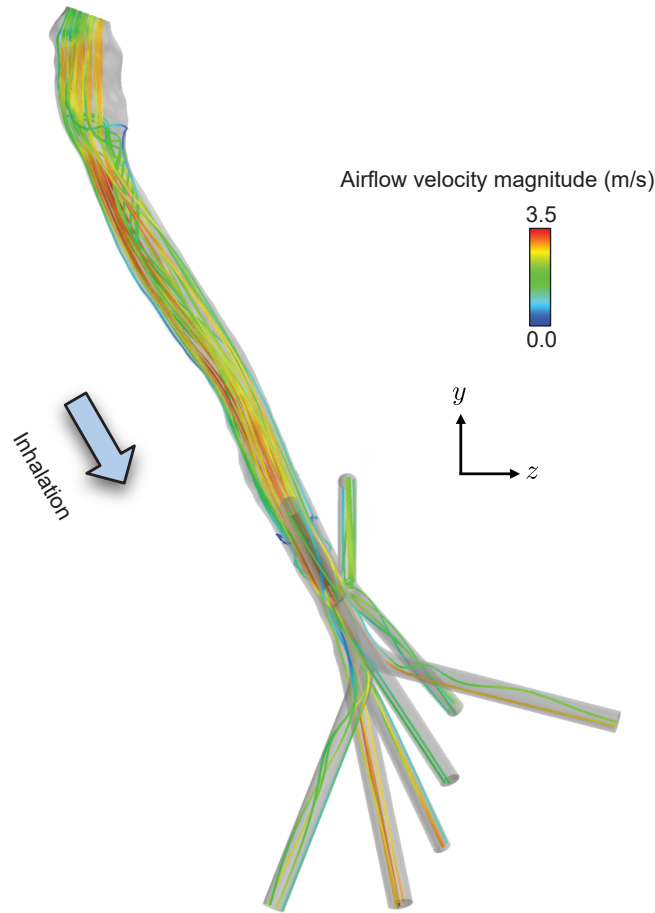


FIG. 4. 30 representative velocity streamlines extracted from the numerically simulated inhaled airflow field.

orientation of the test anatomical cavity) with speed U and at an angle of $\theta_2 = 33.94^\circ$ with respect to the S-ROAM's α -axis, mimicking the simulated motion of particles entering the region; see Fig. 3c. As representative examples, particulate trajectories were derived for two initial positions at the mid-point and near the right edge of the reduced channel's inlet span, and for seven different particulate diameters, namely, 5, 10, 15, 20, 25, 30, and (as an extremal case) $50 \mu\text{m}$.

C. Connecting the fluid dynamics outcomes to virology

From the numerical experiments, this study has deduced the simulated deposition and penetration efficiencies of the particulates along the bronchial tubes (see Table I) and evaluated the respective volumetric transmission to the bronchi. The projected net deposited (at the primary and tertiary bronchi) and penetrated (moving into the respiratory bronchioles) volumes are then multiplied with the sputum viral concentration for a specific pathogen (in this study, SARS-CoV-2) to evaluate and compare the viral load transported via inhaled aerial advection of URT-derived liquid particulates to the lower airway and deep lungs, for select test particulate sizes, namely, 1, 5, 10, and $15 \mu\text{m}$.

Note that the average sputum viral concentration for SARS-CoV-2 has been reported as $\mathcal{V} = 7.0 \times 10^6$ virions/ml, through count measurements of the RNA copies for the single-stranded virus present in the airway liquid samples collected from hospitalized COVID-19 patients [7].

TABLE I. **Numerically simulated bronchial deposition and penetration data:** The particulate sizes, that have been explored further in Table II (to formalize the viral transmission trends as a function of the microdroplet dimensions), are in bold font. *Symbols:* d = tested aerosol (or, droplet) diameter; \mathcal{N} = total number of aerosols/droplets tracked for each particulate diameter; n_p = number of deposited particulates in the primary bronchi; n_t = number of deposited particulates in the tertiary bronchi; n_d = number of particulates penetrating into the respiratory bronchioles toward the deep lungs; η = deposition (or, penetration) rate (in %) to the bronchial pathways.

Separated aerosol/droplet size (d , in μm)	\mathcal{N}	n_p	n_t	n_d	Lung penetration (η , in %)
1	1622	11	0	1611	100.00
2	1622	4	0	1617	99.94
3	1622	14	0	1608	100.00
4	1622	16	0	1606	100.00
5	1622	32	3	1587	100.00
6	1622	83	13	1526	100.00
7	1622	123	25	1469	99.69
8	1622	170	41	1381	98.15
9	1622	173	34	1291	92.36
10	1622	210	41	1183	88.41
11	1622	269	47	1054	84.46
12	1622	316	43	933	79.65
13	1622	369	47	797	74.78
14	1622	420	88	607	68.74
15	1622	461	93	433	60.85
16	1622	489	89	293	53.70
17	1622	460	91	217	47.35
18	1622	417	99	144	40.69
19	1622	365	91	80	33.05
20	1622	324	78	37	27.07
21	1622	280	59	17	21.95
22	1622	221	48	12	17.32
23	1622	172	17	10	12.27
24	1622	120	4	1	7.71
25	1622	81	3	0	5.18
26	1622	57	1	0	3.58
27	1622	38	0	0	2.34
28	1622	20	0	0	1.23
29	1622	5	0	0	0.31
30	1622	0	0	0	0.00

III. RESULTS

A. Bronchial deposition and deep lung penetration as projected from numerical modeling

Figure 4 presents sample inhaled airflow velocity streamlines from the numerical simulation of inhaled airflow passing through the CT-reconstructed anatomical cavity. The simulated inhalation rate of 15 L/min to mimic relaxed breathing warranted an inlet-to-outlet pressure gradient of -9.5 Pa. Against the flow field, the test particulates were tracked with their starting locations uniformly distributed on the cross-sectional space spanning the vocal fold region of the laryngeal cavity (commensurate with their hypothesized formation sites at the URT—through break-up of mucus strata along the nasopharynx, the oropharynx, and the vocal folds).

Table I details the lower airway deposition and penetration data for the tested particulates bearing diameters 1 – 30 μm (with increments of 1 μm). While it is expected that the particulates $\lesssim 5 \mu\text{m}$ would relatively comfortably penetrate to the deep lungs (as is clearly the case per Table I), the high transmission percentages, e.g., for even the 10- and 15- μm particulates is striking—they being 88.41% and 60.85%, respectively. In the table (for 1622 particulates tracked for each size), n_p quantifies the number of particulates depositing in the primary bronchi, n_t quantifies the number of particulates depositing at the tertiary bronchi, and n_d measures the number of particulates escaping through the respiratory bronchiolar outlets of the in silico model and subsequently moving into the deeper recesses of the lungs. See Fig. 1 to review the anatomical zone nomenclature for this study and the respective locations of the different physiological regions along the airway.

TABLE II. **Magnitude of viral load transmission into bronchial pathways as a function of inhaled particulate sizes:** The duration in consideration is 3 days, with a conservative estimate of 1 particulate of each test size generated during each breathing cycle. The breathing cycles last 5 s [39].

Separated aerosol/droplet size (d , in μm)	Number of virions ferried to the bronchial pathways (L_v)
15	390
10	168
5	24
1	0

B. Viral load transmitted to the lower airway

Table II lists the viral load transmitted to the bronchial pathways, for the representative test particulate sizes 1, 5, 10, and 15 μm . For the time scale T (in hours) over which the viral load transmission is to be estimated, we have used 3 days (i.e., 72 hours) based on reported data [38] on the typical time interval that has revealed confirmed infection onset in the deep lungs subsequent to the emergence of initial symptoms along the URT. Further, applying $\delta t = 5$ s as the average duration for a complete breathing cycle [39], the viral load, L_v , transmitted to the bronchial pathways and deep lungs can be computed as:

$$L_v = \frac{144 \pi d^3 \eta T \mathcal{V} \mathcal{P}(d_i)}{\delta t} \times 10^{-12}. \quad (16)$$

where $\mathcal{P}(d_i)$ is the particle size density function that quantifies the number of microdroplets of size d_i generated during each inhalation cycle. For simplicity, the data in Table II enforced $\mathcal{P} = 1$, irrespective of the particulate size, i.e., the particulate formation rate was conservatively assumed to be 1 per breathing cycle, for each test particulate size. Finally, note that while the reported numbers in Table II are based on the estimates guided by equation 16, the zero viral load assessment for the 1- μm particulates implies that the corresponding transmission estimate from equation 16 resulted in a fractional number $\ll 1$, and bears no physical significance.

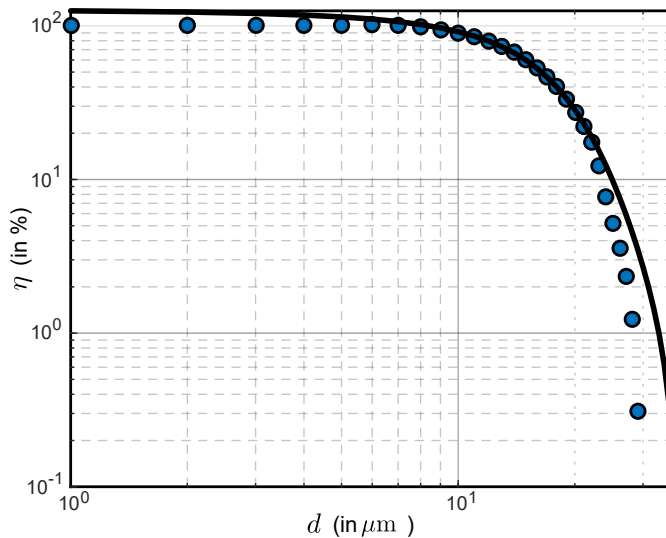


FIG. 5. Log-log plot for η , summing up the bronchial deposition and deep lung penetration percentages (see Table I), for each numerically tracked microdroplet size, d . The simulation-derived data points are marked by the dark blue circles. The solid black line is a fitted curve of the Heaviside step function form (see equation 17).

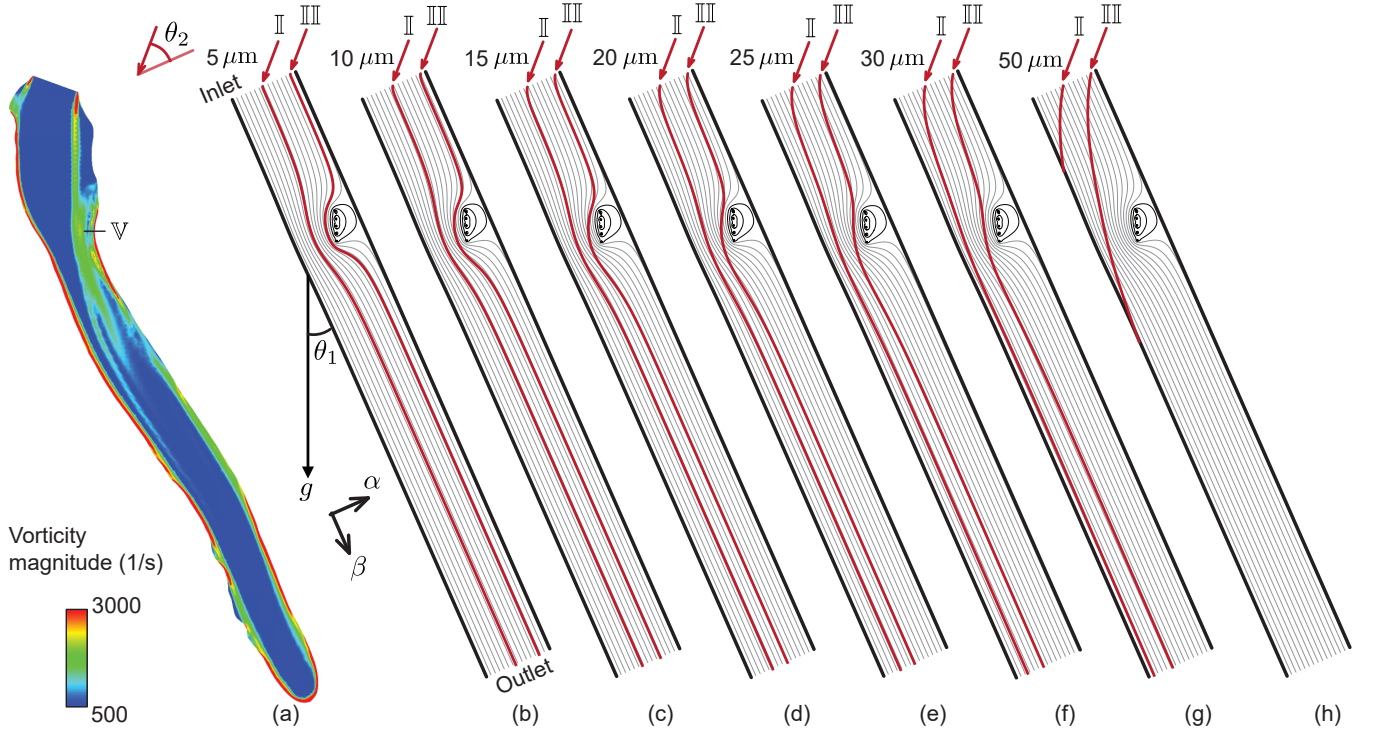


FIG. 6. (a) Simulated vorticity contour map on a representative two-dimensional cross-section (the S-ROAM domain) running approximately midway through the cavity; see Fig. 3b. The region with the dominant vortex core is marked by ∇ . (b-h) show two sample particle pathlines (in red) against the S-ROAM streamlines (in grey), respectively for particle sizes 5, 10, 15, 20, 25, 30, and 50 μm . The black lines on either side of the S-ROAM domain mark the slip wall boundaries. In each case, the vortex patch ∇ is mimicked by a set of five point vortices embedded on a the two-dimensional flow field with background unidirectional flow in the β -direction. The representative particle entering near the middle of the inlet face is marked as II and the particle entering near the right edge of the model channel is marked as III.

C. Heaviside trend governing bronchial deposition and penetration

Collapsing the net particulate transmission efficiencies from Table I, labeled as η (in %), on to a log-log scale with particulate diameters d (in μm) placed along the horizontal axis, reveals (as is expected) a high lower airway penetration for smaller particulate sizes, followed by a gently sloping dip; see Fig. 5. The behavior could be approximately mathematized with a modified Heaviside function [40] of the following analytical form:

$$\eta(d) = C_1 + e^{C_2/[1+e^{2k(d+C_3)}]}, \quad (17)$$

where k and C_i , with $i \in \{1, 2, 3\}$, are constant fitting parameters. For the solid black curve plotted in Fig. 5 and fitting through the data-points from the numerical experiments, the following values were used:

$$C_1 = -1.95, \quad C_2 = 4.95, \quad C_3 = -25.0, \quad k = 0.08. \quad (18)$$

D. Analytical projections for particulate transport: consistent with the full-scale numerical findings

Figure 6a demonstrates the vorticity field mapped over the section shown in Fig. 3c. In the reduced-order analytical setup, the vortex patch marked by ∇ is modeled with a spatial assembly of five point vortices, as described in §II B. In panels b-h of Fig. 6, the grey curves show the streamlines of the background flow field in the S-ROAM, with the red curves tracing the sample particulate trajectories. Smaller particulates, owing to their low inertia and smaller St , follow the streamlines (on which they were embedded at entry points) more closely. For larger particulates, the inertia-dominated dynamics would inhibit downwind penetration through biasing their motion toward wall deposition, e.g., see panels g and (especially) h.

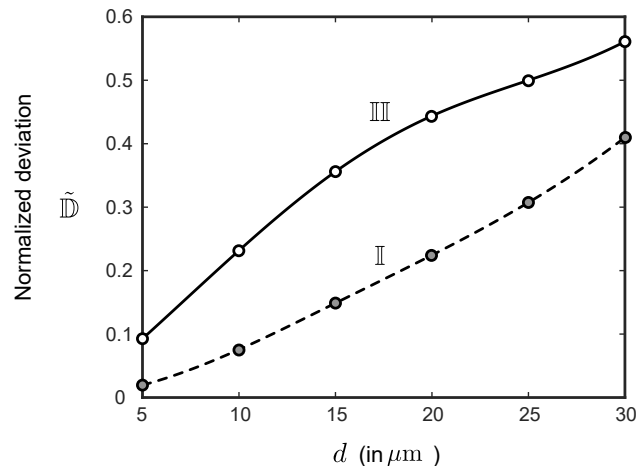


FIG. 7. Comparison of the absolute deviation (\tilde{D} , normalized with respect to the S-ROAM channel width) of the particle pathlines from the respective streamline they were embedded on at the inlet face. The normalized deviation is measured along the α -direction (see Fig. 6). Deviation curves for particles entering near the middle of the S-ROAM inlet face is marked as II and for the particles entering near the right edge of the model channel is marked as III.

Note that the particulates entering through the middle of the inlet face of the S-ROAM are marked as II while those entering near the right edge are marked as III. As shown in Fig. 7, the particulates III, being nearer to the vortex region, are deviated more (from the airflow streamlines they were embedded on at the channel inlet) compared to the particulates II. The deviation generically grows as the particulate diameters are increased, which aligns with the findings in Table I. A greater deviation implies that the particulates are being increasingly shifted toward the channel walls, which in turn would result in a declining deposition and penetration levels in the lower airway.

IV. OPEN QUESTIONS: PERSPECTIVES ON ENHANCING THE BIOPHYSICAL REALISM OF THE MODELING APPROACH

A. On the interfacial mechanics at mucociliary layers during inhalation

While the numerical and analytical models presented here conclude that aerosols/droplets of the length scale $\mathcal{O}(10^1)$ μm , formed through shearing and disintegration of intra-URT mucosal filaments, can have significant deposition and penetration in the deep lungs (e.g., see Table I); to enhance the physiological realism of the model—it is essential that we obtain the actual size distribution and formation rate of liquid particulates generated through viscoelastic separation as the inhaled air brushes past the URT mucus. The present study employed the conservative estimate that 1 particulate of each tested size is formed during each breathing cycle and is a limitation. The reader should however note that unlike expulsion regimes (during exhalation), where imaging-based data collection is relatively straightforward with human subjects expelling particulates into the outside air for different speech and breathing parameters, the current problem of characterizing the internal reverse transport (inhalation) into the lower airway could be somewhat challenging.

With *in vivo* tests in human subjects all but unlikely to receive institutional review board approvals, the approach could be essentially two-fold with synergistic numerical modeling and experimental visualizations. One can consider a 2-phase interaction on anatomically realistic upper airway surfaces; the two phases being the mimicked versions of inhaled air (phase 1) and the relatively static mucosal film (phase 2); see Fig. 8. The interfacial mechanics leading to particulate formation and release, along with their spatiotemporal growth and size distribution, could then be assessed with multiphase simulation techniques. While similar problems in a different context have been studied before—the three-dimensional wavy anatomic topology of the URT surface can potentially reveal interesting nuances related to the dynamics. Experimental visualizations with air flux brushing past a viscoelastic film mimicking mucus rheology should then be able to validate the micro-scale mechanics revealed by the computational approach.

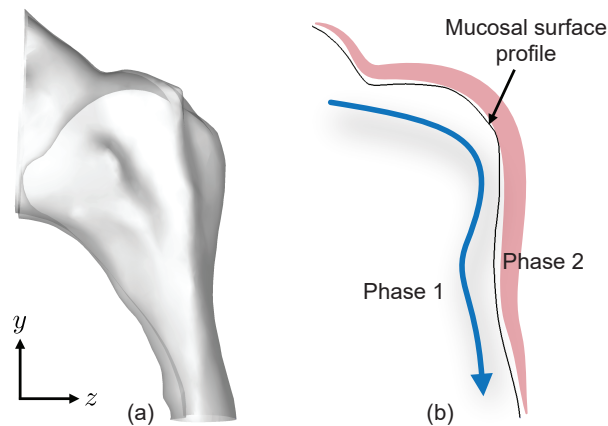


FIG. 8. (a) Nasopharynx (compare with labels on Fig. 1), which is the initial trigger site for SARS infection owing to the propensity of ciliated epithelial cells with angiotensin-converting enzyme 2 (ACE2) surface receptors that the spike protein viruses bind to during cell intrusion. (b) Representative planar outline of the surface topology at the nasopharynx. Phase 1 stands in for the inhaled air flux, phase 2 signifies the mucus film. The blue arrow is a cartooned depiction of the inhaled airflow profile sweeping over the mucosal topography (in pale red). The black curve in panel (b) delineating the mucosal surface topography is extracted from CT data.

B. On experimental validation of deep lung penetration through in vitro physical tests

To verify the numerical modeling of the overall spatial transport, experiments could be conducted in 3D-printed anatomically realistic airway casts that are internally coated with (say) concentrated glycerol (with tuned dilution levels) standing in for mucus. Controlled air flux, with embedded aerosols, could be passed through the cast via suction mechanism set up with a vacuum pump. One approach (amongst others) for getting highly-resolved data on the lower airway penetration could be to use the sophisticated gamma scintigraphy technique [41], wherein the aerosolizing solution to be administered into the three-dimensional cast (with the incoming air) would be seeded with a mildly radioactive element (e.g., Technetium). After the particulates have landed along the airway walls, the radioactive signals (emitted by the deposited mass and hence presenting a measure of local penetration) could be compared with the in silico deposition patterns along the bronchial pathways. Note that for this approach to be functionally consistent, the printed cast should be separable into (at least) two parts along the sagittal mid-section to facilitate controlled liquid coating of its internal surfaces. The separable 3D-printed pieces will also logistically facilitate radio-signal imaging of the wall deposits.

V. CONCLUSION: THE MAIN INFERENCES

A. Can large particulates, generated from the intra-URT mucus coating during inhalation, penetrate to the bronchial airspace?

The particulate transmission trends (see Table I) from the numerical experiments performed in this study are found to be consistent with the first-principles reduced-order analytical findings that modeled the impact of dominant intra-airway vortex instabilities in the laryngotracheal domain on local particle transport (Fig. 6). Clearly, the results establish that not only the aerosols (i.e., particulates with diameters $\lesssim 5 \mu\text{m}$) but also droplets as large as 10 and 15 μm can exhibit remarkable efficiency at reaching the bronchial spaces and deep lungs, so long as they are sheared away from the URT surface and are still airborne as they enter the larynx. This stands in contrast to the general perception that only the particulates that are smaller than 5 μm can penetrate to the lower airway. Missing the nuance therein is the fact that the incumbent perspective is based on the mechanics of particulates inhaled from the outside air, and our understanding of intra-URT mucosal break-up during inhalation and the subsequent aerial advection profiles in the downwind tract is still nascent.

For a physics-based rationale to explain the derived deposition and penetration profiles, let us consider the tortuosity \mathcal{T} of the pathways to be traversed by a particulate inhaled from outside (called hereafter P_o), compared to a particulate that is generated from the URT and is still airborne in the laryngeal airspace (hereafter called P_u). Figure 9 illustrates a representative vertical cutting plane used to extract the tortuosity measurements. For P_o , the corresponding tortuosity

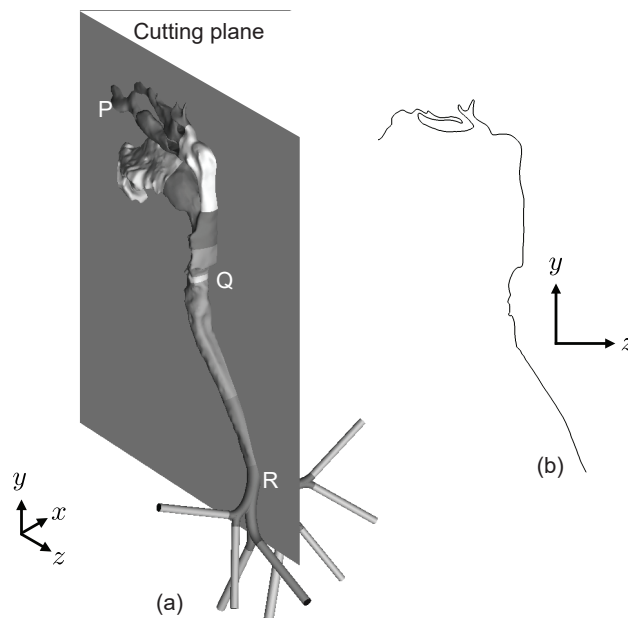


FIG. 9. (a) Sagittal cutting plane through the anatomical airway to extract the intersected curve shown in panel (b) The latter is used to evaluate the tortuosities between P-R and Q-R tracts of the airway.

is the ratio of the curved path length and the linear distance in space between the points P and R; let us represent it as \mathcal{T}_{P_o} . For P_u , it is similarly the ratio of the curved path length and the linear distance in space between the points Q and R; let us represent it as \mathcal{T}_{P_u} . The geometric measurements of the spatial distances return: $\mathcal{T}_{P_o} \approx 1.90$ and $\mathcal{T}_{P_u} \approx 1.04$. Consequently, if the mechanics of P_o is inertia-dominated (true for particulates $\gtrsim 5 \mu\text{m}$), they exhibit less success at navigating the highly tortuous pathway (which would have otherwise led them to the lower airway) and are deposited along the anterior URT. On the contrary, particulates of similar sizes, if they only have to traverse the Q-R tract (see Fig. 7), the less tortuous pathway ensures that a high percentage of them would end up depositing along (or, penetrating to) the bronchial domains. As an aside, also note that the tortuosity estimates obtained here match exactly with our previously published data on mammalian airway morphology with different test airway cavities [42]; see panel (d) in Fig. 1 of the cited article. Thus, the findings from this study satisfactorily address the question Q_1 posed in the introduction (§I), a variant of which is the question heading this subsection.

B. How do the transmitted viral loads compare to the infectious dose of the test pathogen?

Infectious dose, I_D , of a virus quantifies the minimum number of virions that can potentially launch infection in an exposed subject [29, 43] and is a fundamental virological parameter. Independent studies by us [8, 44] and others [9, 45] have verified that $I_D \approx 300$, for SARS-CoV-2 onset. Thus, evidently (per Table II), the viral load transmitted by, e.g., the $15\text{-}\mu\text{m}$ droplets would alone exceed the I_D threshold, thereby providing a mechanics-based rationale for the fast disease progression to the lower airway. The brisk pace is otherwise difficult to explain based exclusively on tissue level proliferation and direct deep lung inhalation of sub $5\text{-}\mu\text{m}$ particulates from outside. However, from a translational paradigm, it is critical to note that the present in silico framework does not *yet* take into account the host innate and adaptive immune responses to the invading virions. The immunological considerations, once incorporated into the mechanics paradigm, can help rationalize the varying rates of clinical prognosis recorded in different subjects [38]; e.g., the deep lung infection for SARS-CoV-2 has historically ensued over a range of 2 – 8 days in different subjects following the appearance of initial symptoms along the upper respiratory tract. In summary, the findings do satisfactorily address the question Q_2 posed in §I, a variant of which is the question heading this subsection.

ACKNOWLEDGMENTS

The author thanks the National Science Foundation for support via the [NSF CAREER Grant, Award No. CBET 2339001](#) (Fluid Dynamics program). The author also thanks Neelesh Patankar (Northwestern University) for stimu-

lating discussions on bronchial fluid mechanics, Julia Kimbell (School of Medicine at the University of North Carolina Chapel Hill) for providing access to existing, de-identified CT imaging, and Abby Wortman (Clinical and Lab Instructor for the Respiratory Care program at the author’s institution) for checking the nomenclature on airway physiology used in this study.

DATA SHARING

Supplemental information (including simulated data, raw files, and codes) are available on-request via [OneDrive](#).

-
- [1] J. A. Moriarty and J. B. Grotberg, Flow-induced instabilities of a mucus–serous bilayer, *Journal of Fluid Mechanics* **397**, 1 (1999).
 - [2] M. Abkarian and H. A. Stone, Stretching and break-up of saliva filaments during speech: A route for pathogen aerosolization and its potential mitigation, *Physical Review Fluids* **5**, 102301 (2020).
 - [3] R. Singhal, S. Ravichandran, R. Govindarajan, and S. S. Diwan, Virus transmission by aerosol transport during short conversations, *Flow* **2** (2022).
 - [4] L. Bourouiba, The fluid dynamics of disease transmission, *Annual Review of Fluid Mechanics* **53**, 473 (2021).
 - [5] C. C. Wang, K. A. Prather, J. Sznitman, J. L. Jimenez, S. S. Lakdawala, Z. Tufekci, and L. C. Marr, Airborne transmission of respiratory viruses, *Science* **373**, eabd9149 (2021).
 - [6] X. Xie, Y. Li, H. Sun, and L. Liu, Exhaled droplets due to talking and coughing, *Journal of the Royal Society Interface* **6**, S703 (2009).
 - [7] R. Wölfel, V. M. Corman, W. Guggemos, M. Seilmaier, S. Zange, M. A. Müller, D. Niemeyer, T. C. Jones, P. Vollmar, C. Rothe, M. Hoelscher, T. Bleicker, S. Brünink, J. Schneider, R. Ehmann, K. Zwirgmaier, C. Drosten, and C. Wendtner, Virological assessment of hospitalized patients with COVID-2019, *Nature* **581**, 465 (2020).
 - [8] S. Basu, Computational characterization of inhaled droplet transport to the nasopharynx, *Scientific Reports* **11**, 1 (2021).
 - [9] K. A. Ryan, K. R. Bewley, S. A. Fotheringham, G. S. Slack, P. Brown, Y. Hall, N. I. Wand, A. C. Marriott, B. E. Cavell, J. A. Tree, L. Allen, M. J. Aram, T. J. Bean, E. Brunt, K. R. Buttigieg, D. P. Carter, R. Cobb, N. S. Coombes, S. J. Findlay-Wilson, K. J. Godwin, K. E. Gooch, J. Gouriet, R. Halkerston, D. J. Harris, T. H. Hender, H. E. Humphries, L. Hunter, C. M. K. Ho, C. L. Kennard, S. Leung, S. Longet, D. Ngabo, K. L. Osman, J. Paterson, E. J. Penn, S. T. Pullan, E. Rayner, O. Skinner, K. Steeds, I. Taylor, T. Tipton, S. Thomas, C. Turner, R. J. Watson, N. R. Wiblin, S. Charlton, B. Hallis, J. A. Hiscox, S. Funnell, M. J. Dennis, C. J. Whittaker, M. G. Catton, J. Druce, F. J. Salguero, and M. W. Carroll, Dose-dependent response to infection with SARS-CoV-2 in the ferret model and evidence of protective immunity, *Nature Communications* **12**, 1 (2021).
 - [10] S. Basu, When fluid mechanics meets virology: a modeling framework for respiratory infection onset and projection of viral infectious dose, in *APS Division of Fluid Dynamics Meeting Abstracts* (2021) pp. A01–001.
 - [11] A. Chakravarty, D. Kundu, M. V. Panchagnula, A. Mohan, and N. A. Patankar, Perspectives on physics-based one-dimensional modeling of lung physiology, arXiv preprint arXiv:2403.09203 (2024).
 - [12] S. Jung, Simplified models of aerosol collision and deposition for disease transmission, *Scientific Reports* **13**, 20778 (2023).
 - [13] O. Erken, B. Fazla, M. Muradoglu, D. Izbassarov, F. Romano, and J. B. Grotberg, Effects of elastoviscoplastic properties of mucus on airway closure in healthy and pathological conditions, *Physical Review Fluids* **8**, 053102 (2023).
 - [14] A. Chen, T. Wessler, K. Daftari, K. Hinton, R. C. Boucher, R. Pickles, R. Freeman, S. K. Lai, and M. G. Forest, Modeling insights into SARS-CoV-2 respiratory tract infections prior to immune protection, *Biophysical Journal* **121**, 1619 (2022).
 - [15] C. Darquenne, A. A. T. Borojeni, M. J. Colebank, M. G. Forest, B. G. Madas, M. Tawhai, and Y. Jiang, Aerosol transport modeling: the key link between lung infections of individuals and populations, *Frontiers in Physiology* **13**, 923945 (2022).
 - [16] A. Chakravarty, M. V. Panchagnula, and N. A. Patankar, Inhalation of virus-loaded droplets as a clinically plausible pathway to deep lung infection, *Frontiers in Physiology* **14**, 1073165 (2023).
 - [17] J. M. Oakes, The utility of hybrid in silico models of airflow and aerosol dosimetry in the lung, *Journal of Biomechanics* , 112126 (2024).
 - [18] J. B. West, *Respiratory Physiology: The Essentials* (Lippincott Williams & Wilkins, 2012).
 - [19] S. Basu, D. O. Frank-Ito, and J. S. Kimbell, On computational fluid dynamics models for sinonasal drug transport: Relevance of nozzle subtraction and nasal vestibular dilation, *International Journal for Numerical Methods in Biomedical Engineering* **34**, e2946 (2018).
 - [20] E. L. Perkins, S. Basu, G. J. M. Garcia, R. A. Buckmire, R. N. Shah, and J. S. Kimbell, Ideal particle sizes for inhaled steroids targeting vocal granulomas: preliminary study using computational fluid dynamics, *Otolaryngology – Head and Neck Surgery* **158**, 511 (2018).
 - [21] S. Basu, N. Witten, and J. S. Kimbell, Influence of localized mesh refinement on numerical simulations of post-surgical sinonasal airflow, *Journal of Aerosol Medicine and Pulmonary Drug Delivery* **30**, A (2017).
 - [22] D. C. Wilcox, *Turbulence modeling for CFD*, Vol. 2 (DCW industries La Canada, CA, 1998).

- [23] W. W. Kim and S. Menon, Application of the localized dynamic subgrid-scale model to turbulent wall-bounded flows, in *35th Aerospace Sciences Meeting and Exhibit* (1997) p. 210.
- [24] N. Baghernezhad and O. Abouali, Different SGS models in Large Eddy Simulation of 90° square cross-section bends, *Journal of Turbulence*, N50 (2010).
- [25] E. Ghahramani, O. Abouali, H. Emdad, and G. Ahmadi, Numerical investigation of turbulent airflow and microparticle deposition in a realistic model of human upper airway using LES, *Computers & Fluids* **157**, 43 (2017).
- [26] J. Jovanovic and I. Otic, On the constitutive relation for the reynolds stresses and the prandtl-kolmogorov hypothesis of effective viscosity in axisymmetric strained turbulence, *Journal of Fluids Engineering* **122**, 48 (2000).
- [27] G. J. M. Garcia, J. D. Schroeter, R. A. Segal, J. Stanek, G. L. Foureman, and J. S. Kimbell, Dosimetry of nasal uptake of water-soluble and reactive gases: a first study of interhuman variability, *Inhalation Toxicology* **21**, 607 (2009).
- [28] S. A. J. Morsi and A. J. Alexander, An investigation of particle trajectories in two-phase flow systems, *Journal of Fluid mechanics* **55**, 193 (1972).
- [29] V. Stadnytskyi, C. E. Bax, A. Bax, and P. Anfinrud, The airborne lifetime of small speech droplets and their potential importance in SARS-CoV-2 transmission, *Proceedings of the National Academy of Sciences* **117**, 11875 (2020).
- [30] H. Fischer, I. Polikarpov, and A. F. Craievich, Average protein density is a molecular-weight-dependent function, *Protein Science* **13**, 2825 (2004).
- [31] S. Basu, L. P. Chamorro, M. Yeasin, and M. A. Stremmer, Modeling the effect of vorticity on inhaled transport in the upper airway, arXiv preprint arXiv:2406.09708 (under review, 2024).
- [32] A. Friedmann and P. Poloubarinova, Über fortschreitende singularitäten der ebenen bewegung einer inkompressiblen flüssigkeit, *Recueil de Géophysique* **5**, 9 (1928).
- [33] H. Aref, Point vortex dynamics: a classical mathematics playground, *Journal of Mathematical Physics* **48** (2007).
- [34] S. Basu and M. A. Stremmer, Exploring the dynamics of ‘2P’ wakes with reflective symmetry using point vortices, *Journal of Fluid Mechanics* **831**, 72 (2017).
- [35] M. R. Maxey and J. J. Riley, Equation of motion for a small rigid sphere in a nonuniform flow, *Physics of Fluids* **26**, 883 (1983).
- [36] A. Babiano, J. H. E. Cartwright, O. Piro, and A. Provenzale, Dynamics of a small neutrally buoyant sphere in a fluid and targeting in Hamiltonian systems, *Physical Review Letters* **84**, 5764 (2000).
- [37] P. Tallapragada and S. D. Ross, Particle segregation by Stokes number for small neutrally buoyant spheres in a fluid, *Physical Review E* **78**, 036308 (2008).
- [38] Y. J. Hou, K. Okuda, C. E. Edwards, D. R. Martinez, T. Asakura, K. H. Dinno III, T. Kato, R. E. Lee, B. L. Yount, T. M. Mascenik, G. Chen, K. M. Olivier, A. Ghio, L. V. Tse, S. R. Leist, L. E. Gralinski, A. Schäfer, H. Dang, R. Gilmore, S. Nakano, L. Sun, M. L. Fulcher, A. Livraghi-Butrico, N. I. Nicely, M. Cameron, C. Cameron, D. J. Kelvin, A. de Silva, D. M. Margolis, A. Markmann, L. Bartelt, R. Zumwalt, F. J. Martinez, S. P. Salvatore, A. Borczuk, P. R. Tata, V. Sontake, A. Kimple, I. Jaspers, W. K. O’Neal, S. H. Randell, R. C. Boucher, and R. S. Baric, SARS-CoV-2 Reverse Genetics Reveals a Variable Infection Gradient in the Respiratory Tract, *Cell* (2020).
- [39] RESPe, Normal breathing, [Web link](#) (accessed 23-March-2024).
- [40] K. F. Riley, M. P. Hobson, and S. J. Bence, *Mathematical methods for Physics and Engineering* (Cambridge University Press, 2004).
- [41] S. Basu, L. T. Holbrook, K. Kudlaty, O. Fasanmade, J. Wu, A. Burke, B. W. Langworthy, Z. Farzal, M. Mamdani, W. D. Bennett, J. P. Fine, B. A. Senior, A. M. Zanation, C. S. Ebert Jr, A. J. Kimple, B. D. Thorp, D. O. Frank-Ito, G. J. M. Garcia, and J. S. Kimbell, Numerical evaluation of spray position for improved nasal drug delivery, *Scientific Reports* **10**, 1 (2020).
- [42] J. Yuk, A. Chakraborty, S. Cheng, C. I. Chung, A. Jorgensen, S. Basu, L. P. Chamorro, and S. Jung, On the design of particle filters inspired by animal noses, *Journal of the Royal Society Interface* **19**, 1 (2022).
- [43] M. P. Zwart, L. Hemerik, J. S. Cory, J. A. G. M. de Visser, F. J. J. A. Bianchi, M. M. Van Oers, J. M. Vlak, R. F. Hoekstra, and W. Van der Werf, An experimental test of the independent action hypothesis in virus–insect pathosystems, *Proceedings of the Royal Society B: Biological Sciences* **276**, 2233 (2009).
- [44] S. Basu, Recent results on droplet transmission in the upper airway leading to SARS-CoV-2 infection and an estimation of the infectious dose, in *Proceedings of the XXV Intenational Congress of Theoretical and Applied Mechanics (ICTAM) (IUTAM, 2020+1)*.
- [45] M. Prentiss, A. Chu, and K. K. Berggren, Finding the infectious dose for COVID-19 by applying an airborne-transmission model to superspreader events, *PLOS One* **17**, e0265816 (2022).